

Airborne geophysical surveys of the lower Mississippi Valley demonstrate system-scale mapping of subsurface architecture

Burke J. Minsley ¹✉, J. R. Rigby ², Stephanie R. James ¹, Bethany L. Burton ¹, Katherine J. Knierim³, Michael D. M. Pace ¹, Paul A. Bedrosian ¹ & Wade H. Kress⁴

The Mississippi Alluvial Plain hosts one of the most prolific shallow aquifer systems in the United States but is experiencing chronic groundwater decline. The Reelfoot rift and New Madrid seismic zone underlie the region and represent an important and poorly understood seismic hazard. Despite its societal and economic importance, the shallow subsurface architecture has not been mapped with the spatial resolution needed for effective management. Here, we present airborne electromagnetic, magnetic, and radiometric observations, measured over more than 43,000 flight-line-kilometers, which collectively provide a system-scale snapshot of the entire region. We develop detailed maps of aquifer connectivity and shallow geologic structure, infer relationships between structure and groundwater age, and identify previously unseen paleochannels and shallow fault structures. This dataset demonstrates how regional-scale airborne geophysics can close a scale gap in Earth observation by providing observational data at suitable scales and resolutions to improve our understanding of subsurface structures.

¹US Geological Survey, Geology, Geophysics, and Geochemistry Science Center, Denver, CO, USA. ²US Geological Survey, Lower Mississippi-Gulf Water Science Center, Oxford, MS, USA. ³US Geological Survey, Lower Mississippi-Gulf Water Science Center, Little Rock, AR, USA. ⁴US Geological Survey, Lower Mississippi-Gulf Water Science Center, Nashville, TN, USA. ✉email: bminsley@usgs.gov

Groundwater is the world's most extracted raw material, with annual withdrawals of 600–1100 km³/year^{1,2}. Withdrawals from freshwater aquifers supply nearly half of the world's drinking water and 43% of water for irrigation^{1,3}. Increasing withdrawals from finite groundwater stores driven by changes in the availability of clean surface water, climate, population growth, and management have led to significant stress on global groundwater systems^{4–6}. Despite the critical importance of groundwater, aquifers remain a largely hidden resource that have not received the level of detailed exploration typically given to other natural resources such as oil and gas reservoirs⁵.

Groundwater withdrawals for irrigation made up ~20% of the total freshwater use for 2015 in the United States, of which 58% was extracted from the High Plains (HP, 20.3%), Mississippi Alluvial Plain (MAP, 20.5%), and Central Valley (CV, 17.7%) aquifer systems (Fig. 1a)^{7,8}. Sustained withdrawals in the MAP region have led to significant groundwater-level declines in excess of 100 feet (30 m) from pre-development conditions before significant groundwater pumping in the mid-twentieth century through 2007, primarily in Arkansas and Mississippi⁹. The Mississippi River Valley alluvial aquifer (MRVA), the surficial aquifer within the MAP region, was among the most heavily withdrawn aquifers for irrigation in 2015 (11.7 Bg/day)⁷ (Fig. 1a). Approximately 8 million acres (32% of the MRVA footprint) are irrigated¹⁰, with the overwhelming majority derived from the shallow, highly productive MRVA. The total revenue and economic impact of row crop agriculture were nearly \$12 billion in 2017¹¹.

Groundwater management over large regions often relies on scant data about the structure, extent, and connectivity of principal freshwater aquifers. The most detailed information about aquifer structure often comes from an ad hoc collection of borehole data acquired for disparate purposes over years to decades from various sources such as municipal, irrigation, or resource exploration wells, and is curated by multiple agencies, with no official central repository or common data standards. Regional-scale borehole information is highly variable in its spatial coverage, content, and data quality. Borehole data do not uniformly sample the subsurface either in land area or in depth, and information about data uncertainty is often missing or anecdotal. The need for consistent and spatially extensive data has led to rapid advancement in the use of remote sensing techniques. For example, advances in satellite and

high-altitude airborne remote sensing methods have dramatically advanced our ability to understand water use and water budgets at regional to global scales^{12–15}. Together with ground-based observations, remotely sensed data of changes at the Earth's surface are greatly improving the predictive capabilities of groundwater simulations¹⁶.

Airborne electromagnetic (AEM) methods are emerging as a highly cost-effective means for extending remote sensing capabilities to the characterization of the subsurface at the watershed to basin scale, filling a critical scale gap in Earth observation between ground-based and satellite or airborne remote sensing methods (Fig. 1b). AEM has been applied to groundwater studies for decades^{17–24}, with numerous applications in studies of the cryosphere^{25–27}, infrastructure²⁸, and hazards^{29,30}. However, most AEM studies have been applied to relatively limited areas (a few hundred to a few thousand square kilometers) that represent only part of a larger geological or hydrological system. In this study, we present the first AEM effort to map an entire major aquifer system in the United States, covering >140,000 km² within the MAP region.

The modern lower Mississippi River valley has primarily been shaped by the combined forces of glaciation and sea-level change^{31–33}. Between 2.4 Ma and 250 ka, erosion removed a thick sequence of Pliocene gravels along with tens of meters of underlying earlier Tertiary sediments³⁴, leaving <100 m of discontinuous Pleistocene sediments unconformably overlying a thick sequence of Cretaceous–Tertiary sediments of the Mississippi Embayment^{35,36}. These Pliocene gravels are preserved only at higher elevations in a small area on Crowley's Ridge and outside the footprint of the MRVA^{34,37}. Borehole data provide constraints on the thickness of Quaternary MRVA sediments^{38,39}, and optically stimulated luminescence (OSL) measurements helped to refine the chronology of the valley over the last glacial cycle during the past ~100 ka^{33,40}. In the northern part of the MAP study area, tectonic activity associated with faults of the Cambrian Reelfoot rift (RR) has caused deformation of the Pliocene–Pleistocene unconformity that forms the base of the alluvial aquifer system. Fault activity and uplift have continued in the Quaternary with implications for modern-day hydrologic systems^{34,41} as well as seismicity related to the New Madrid seismic zone (NMSZ)⁴².

The US Geological Survey's MAP Regional Water Availability Study began in 2016 to pilot a next-generation approach to

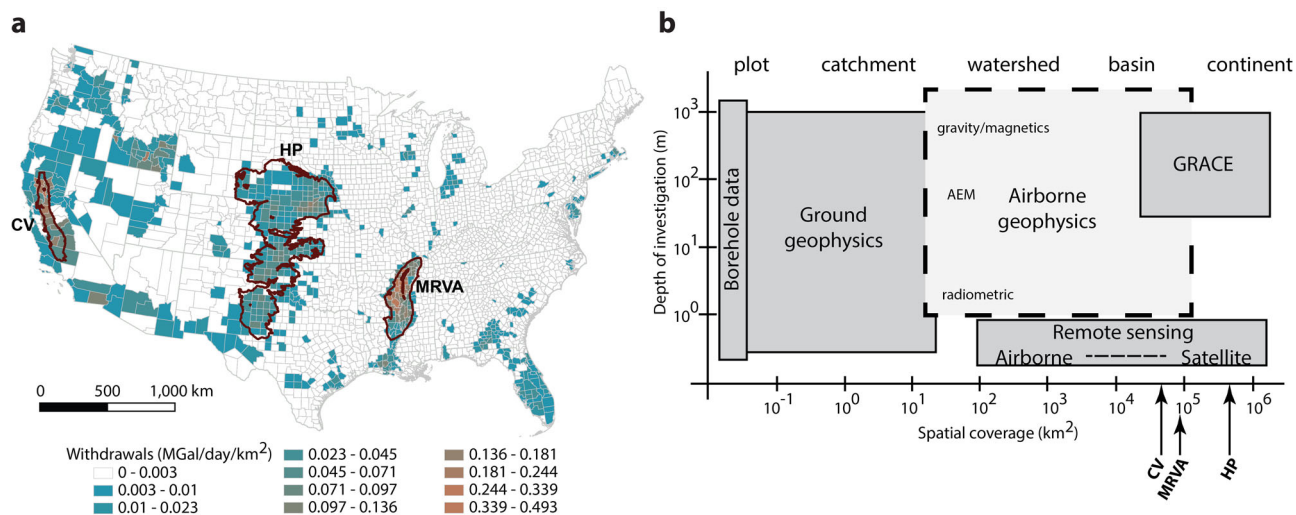


Fig. 1 Large-scale withdrawals of groundwater from major US aquifers require system-scale methods for subsurface characterization. **a** Groundwater withdrawals for irrigation and aquaculture in 2015 by county⁸ highlight the three most heavily produced US aquifers, HP High Plains, CV Central Valley, and MRVA Mississippi River Valley alluvial aquifer. **b** Methods for characterization of surface and subsurface properties from plot to continental scales illustrate the critical scale gap filled by airborne geophysical methods.

integrated water availability assessments. Original development of the hydrogeologic framework for the earlier Mississippi Embayment Regional Aquifer Study (MERAS) model⁴³ incorporated >2600 geophysical logs and well data within the Mississippi Embayment⁴⁴ focused on the deeper Tertiary units that are primarily used for drinking water. Borehole constraints on the surficial MRVA have been sparse by comparison because of its primary use as an irrigation source. Out of the available 2652 boreholes, only 381 were able to define the base of the MRVA, or roughly one control point for every 200 km². As part of the new MAP assessment, a regional AEM survey was designed as the foundation for updating the hydrogeologic framework of the MRVA together with updated borehole compilations^{39,41}.

In this first-of-its-kind regional AEM study, we demonstrate the utility of airborne geophysical data for improving understanding of the structure of the surficial aquifer and surrounding geological formations that are of critical importance not only for effective water resource management in the region but also have broader implications for geologic mapping and hazards investigations. Our data refine system-scale detail of the MRVA, surficial confining material, and the configuration of deeper Tertiary units to improve understanding of regional hydrology. High-resolution

flight-line data and grids reveal previously unseen features such as buried paleochannels in Mississippi and faults adjacent to the NMSZ in Arkansas and Missouri—structures that have potential for significant impact on the Earth system compared with their relatively small footprint (which makes detection difficult) within the larger study area. Beyond the results presented here, we expect these system-scale data and models will have broad community value for comprehensive and diverse investigations of the MAP region going forward, and demonstrate the value of taking a regional approach to understanding the subsurface that is foundational to many scientific and societal studies.

Results and discussion

A system-scale airborne geophysical survey. From 2018 through early 2020, we acquired more than 43,000 flight-line-kilometers (line-km) of airborne geophysical data over the MAP study area of ~140,000 km² (Fig. 2a, “Methods” section). Data collection included a high-resolution survey over ~1000 km² near Shellmound, Mississippi, regional surveys with 3–6 km line spacing across the entire study area, and over 3000 line-km of data acquired along streams and rivers to characterize potential surface

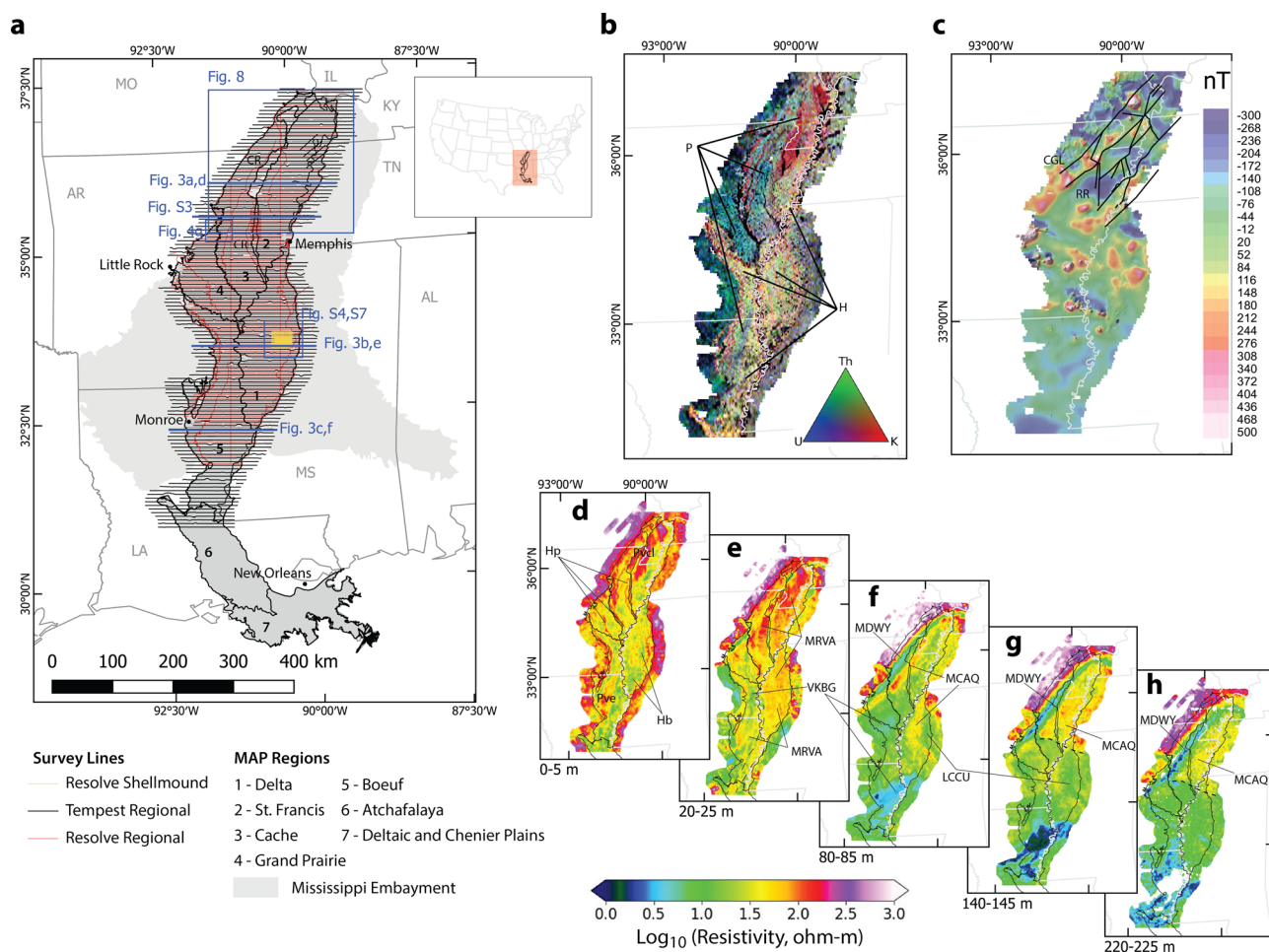


Fig. 2 Airborne geophysical survey coverage and summary of regional datasets. **a** Primary management regions in the MAP study area, with flight lines for each of the three phases of data collection completed through early 2020 (CR Crowleys Ridge). Results from the combined regional surveys gridded onto the 1 km National Hydrogeologic Grid⁴⁵ include **b** radiometric data presented as a ternary diagram that indicates the relative abundance of K, U, and Th in surficial sediments with areas of Holocene (H)- and Pleistocene (P)-aged sediments indicated³²; **c** the residual magnetic intensity map (in nanoTeslas, nT) shows faults⁴⁶ related to the New Madrid seismic zone (RR Reelfoot rift, CGL Commerce geophysical lineament); and **d-h** resistivity depth slices at five depth intervals from 0 to 220 m below land surface annotated with mapped surficial geologic units³² (Hb backswamp, Hp Point bar and meander belt, Pve & Pvc Wisconsin-age valley train) and four-letter codes of distinguishable hydrogeologic units (MRVA Mississippi River Valley alluvial aquifer, VKBG Vicksburg–Jackson confining unit, MCAQ Middle Claiborne aquifer, LCCU Lower Claiborne confining unit, MDWY Midway confining unit).

water–groundwater connections beneath these important recharge pathways. Radiometric (Fig. 2b), magnetic (Fig. 2c), and inverted resistivity grids at multiple depth intervals (Fig. 2d–h) summarize the combined results from both regional survey phases. Together, this represents the first initiative to acquire system-scale airborne geophysical data over an entire US aquifer.

At the regional scale, radiometric data (Fig. 2b) correlate with mapped surficial geology³² and sediment age, with Holocene deposits clearly delineated as strong returns of multiple elements (light-colored areas in Fig. 2b) compared with Pleistocene sediments. Magnetic data gridded at this scale largely corroborated previously mapped structures, such as the line of southwest–northeast-trending magnetic highs (Fig. 2c) associated with mapped intrusive plutons along the Commerce geophysical lineament (CGL) adjacent to the RR in northeast Arkansas and southeast Missouri^{45,46}.

Inverted resistivity models in the uppermost 5 m (Fig. 2d and Fig. S1b) correspond closely with mapped surficial units³² (Fig. S1a). For example, Wisconsin-age valley train deposits, as well as point bars and meander scrolls of modern river networks, appear as resistive features in the uppermost 5 m, whereas fine-grained units such as backswamp deposits are characterized by low resistivity. At 20–25 m depth (Fig. 2e and Fig. S1c), intermediate to high-resistivity values are consistent with the coarse-grained lithology found throughout the MRVA. Lower resistivity can be found at this depth in sedimentary units outside the MAP region as well as over structural highs within the MAP region where Tertiary units are close to the surface. Low-resistivity values show the Vicksburg–Jackson confining unit (VKBG) in southeast Arkansas and northeast Louisiana, the Midway confining unit (MDWY) in northeast Arkansas, and an erosional remnant of Tertiary sediments beneath Crowleys Ridge. Beneath the Quaternary MRVA (~30–50 m depth in most of the region), resistivity values strongly correlate with Tertiary subcropping units (Fig. 2f–h and Fig. S1d, e). Most notable here is the low resistivity that corresponds with the known regional VKBG and MDWY confining units, both clay and shale rich. In contrast, the subcrop of the Middle Claiborne aquifer (MCAQ)

sands are resistive (Fig. 2g, h and Fig. S1d), with a notable change in facies north of Memphis, Tennessee, associated with the coarse Memphis Sand of the Claiborne Group (dashed line, Fig. 2g, h).

Further correlation between resistivity and geologic structure is evident in cross-section view (Fig. 3a–c), where gridded resistivity models are compared with the top elevation of MERAS model surfaces⁴³. From west to east, prominent features in Fig. 3a include the highly resistive Paleozoic Ozark Plateaus aquifer that bounds the MAP region, the conductive east-dipping MDWY beneath and west of Crowleys Ridge, and the resistive MCAQ dipping to the east beneath the east side of Crowleys Ridge. This section highlights the variable degree of connectivity between the MRVA and underlying Tertiary aquifers. While the MCAQ sands appear connected to the shallow MRVA (veneer of moderate to high resistivity in the upper 30–50 m) immediately east of Crowleys Ridge, these aquifer layers become mostly separated by the Middle Claiborne confining unit (MCCU) farther east. To the south (Fig. 3b), the subcrop of the Claiborne Group aquifers (MCAQ and Upper Claiborne aquifer) suggests a direct connection to the MRVA beneath the Mississippi Delta, sandwiched between the VKBG confining unit in the shallow western half of the section and the Lower Claiborne confining unit (LCCU) that dips westward in the eastern part of the section. Towards the southern end of the AEM survey (Fig. 3c), the MRVA is disconnected from Tertiary aquifers by the MCCU and VKBG confining units in the western and eastern portions of the section, respectively. AEM-derived resistivity models largely corroborate the existing framework but also reveal greater detail in the overall structure and heterogeneity within units than could be previously determined through relatively sparse borehole observations. This study demonstrates that systematic mapping at high spatial resolution with AEM data illuminates model structural details expected to exist throughout the region but that cannot be fully understood with sparse observations.

Combined resistivity models from the two phases of regional data collection (Fig. 2d–h and Fig. 3a–c) have been interpolated onto grids with 1 km × 1 km lateral and 5-m vertical resolution useful for investigation of regional-scale structure. However, the

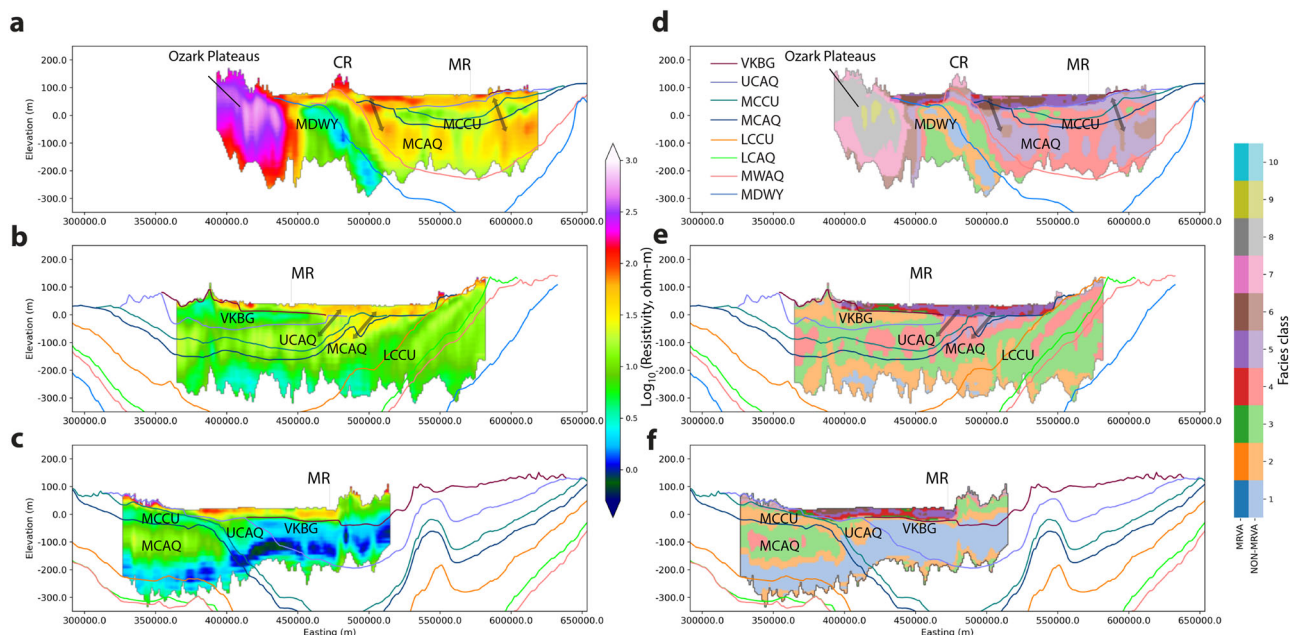


Fig. 3 Resistivity and interpreted facies classification cross-sections. West–east resistivity (a–c) and facies classification (d–f) sections are shown at three latitudes across the survey area (Fig. 2a). Surfaces of the top elevation of MERAS model hydrogeologic units⁴³ are shown on cross-sections for reference. CR Crowleys Ridge, MR Mississippi River. Two-sided arrows indicate potential regions of connectivity between MRVA and deeper aquifer units.

native resolution of resistivity models along flight paths is much higher, with spacing between sounding locations for the Resolve and Tempest AEM systems equal to 25 and 75 m, respectively, with finer-scale near-surface vertical resolution for the Resolve system. On a native-resolution cross-section of the Resolve system in northeast Arkansas (Fig. S2), significant detail reveals the internal structure and variability of the MRVA. For example, the Resolve models capture the topography of the aquifer base, including incised channels in the subcropping Tertiary unit that may have been formed during periods of glacial outwash (interpreted locations marked “C” on Fig. S2), and the thickness and extent of surficial low-resistivity material that may be local confining units and a barrier to recharge. Lateral transitions in the upper ~5–30 m correspond with mapped braid belts³³, suggesting that electrical resistivity can be an indicator of these distinct lithologic units. However, since the chronology of mapped braid belts is largely based on relatively shallow OSL dates and surficial mapping³³, there is little constraint on the age of deeper Quaternary sediments beyond the estimate of their deposition after 250 ka³⁴. Given the

presence of shallow braid belt deposits older than the last sea-level lowstand ~20 ka³³, along with the observed internal structure of the MRVA with a discontinuous low-resistivity layer at ~30 m (Fig. S2), we hypothesize that the deeper Quaternary sediments may represent earlier filling of post-250 ka eroded channels of the ancestral Mississippi–Ohio River systems^{34,38}.

Derivative products: interpretations of hydrogeologic structure and properties. While lithology dominates AEM-derived resistivity values in the MAP region, porewater salinity is also known to influence resistivity^{17,19,24}, and groundwater salinity varies throughout the study area^{47,48}. Specific conductance (SC) measured in boreholes throughout the MERAS domain are generally low, with similar values in both Quaternary sediments (median log₁₀ SC 2.79 = 617 μS/cm) and deeper Tertiary units (median log₁₀ SC 2.67 = 471 μS/cm). Areas of high salinity are limited within the MRVA footprint, with only 6% of the area predicted to be >1000 μS/cm⁴⁸. Correlation between SC- and AEM-derived resistivity (Fig. 4) by

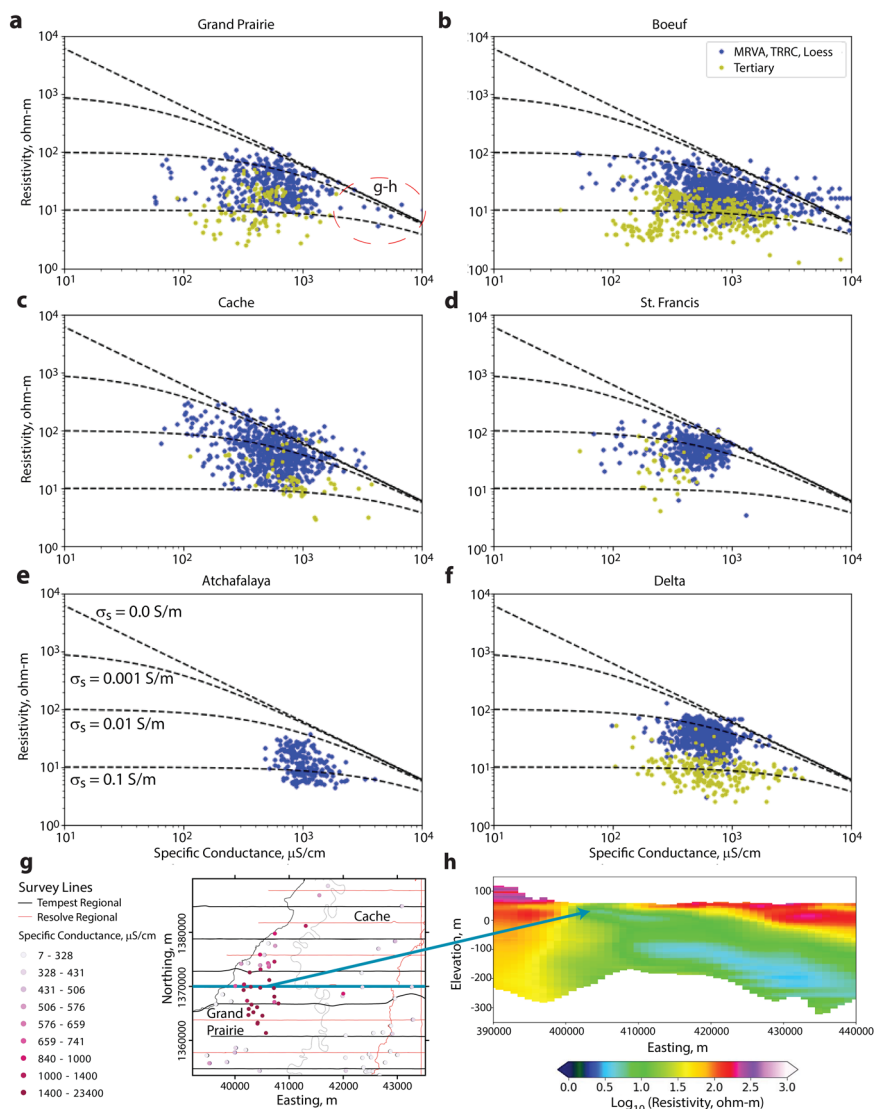


Fig. 4 Relationships between groundwater salinity and AEM-derived resistivity. a–f Measured groundwater specific conductance (SC) versus AEM-derived resistivity at borehole locations, organized by region (Fig. 2). SC measurements from MRVA, terrace (TRRC), and loess layers are shown in blue, with measurements from deeper Tertiary units in yellow. Black dashed curves illustrate theoretical SC-resistivity relationships for varying amounts of surface conductivity (σ_s) caused by the increasing fraction of fine-grained sediment. g Map view of a high-SC cluster in White County, Arkansas, correlates with decreased shallow resistivity in cross-section view (h) and corresponds to the high-SC observations circled in (a).

MAP region (Fig. 2) suggests that SC has limited overall control on resistivity across the study domain, but can be important in specific regions where SC is high, generally in the Grand Prairie (Fig. 4a) and Boeuf (Fig. 4b) regions. Lithology appears to be a primary driver for resistivity, with Quaternary sediments typically higher in resistivity than Tertiary units (Fig. 4a–f) over the same SC range. Tertiary, and to a lesser degree Quaternary, units follow an SC-resistivity trend indicative of moderate-high surface conductivity caused by an increased fraction of clays or other fine-grained sediments that flattens the slope of this relationship (black curves, Fig. 4a–f), compared with Archie’s Law where surface conduction is absent^{49,50}. Notable exceptions where Quaternary and Tertiary resistivity values are similar occur in the Cache (Fig. 4c) and St. Francis (Fig. 4d) regions, where coarse-grained MCAQ sand subcrop beneath the MRVA and appear similar geophysically (double-sided arrow in Fig. 3a just east

of Crowley’s Ridge). The sensitivity of AEM data to both model structure and porewater salinity makes it a powerful tool in hydrologic studies, and also highlights the need for borehole and other geologic observations to calibrate against to reduce uncertainty in the extrapolation of AEM interpretations across the entire survey domain.

Using 6130 published picks defining the depth to the base of the MRVA³⁹ within the AEM survey area, along with an additional 364 manual picks based on observation of resistivity cross-sections, we used a supervised machine learning algorithm⁵¹ (see “Methods” Section) to interpret the elevation of the base of the aquifer across the entire AEM dataset (Fig. 5a). An associated aquifer thickness map (Fig. 5b) is estimated by differencing the base of aquifer elevation surface from the land surface elevation, and saturated thickness (Fig. S3) is calculated by

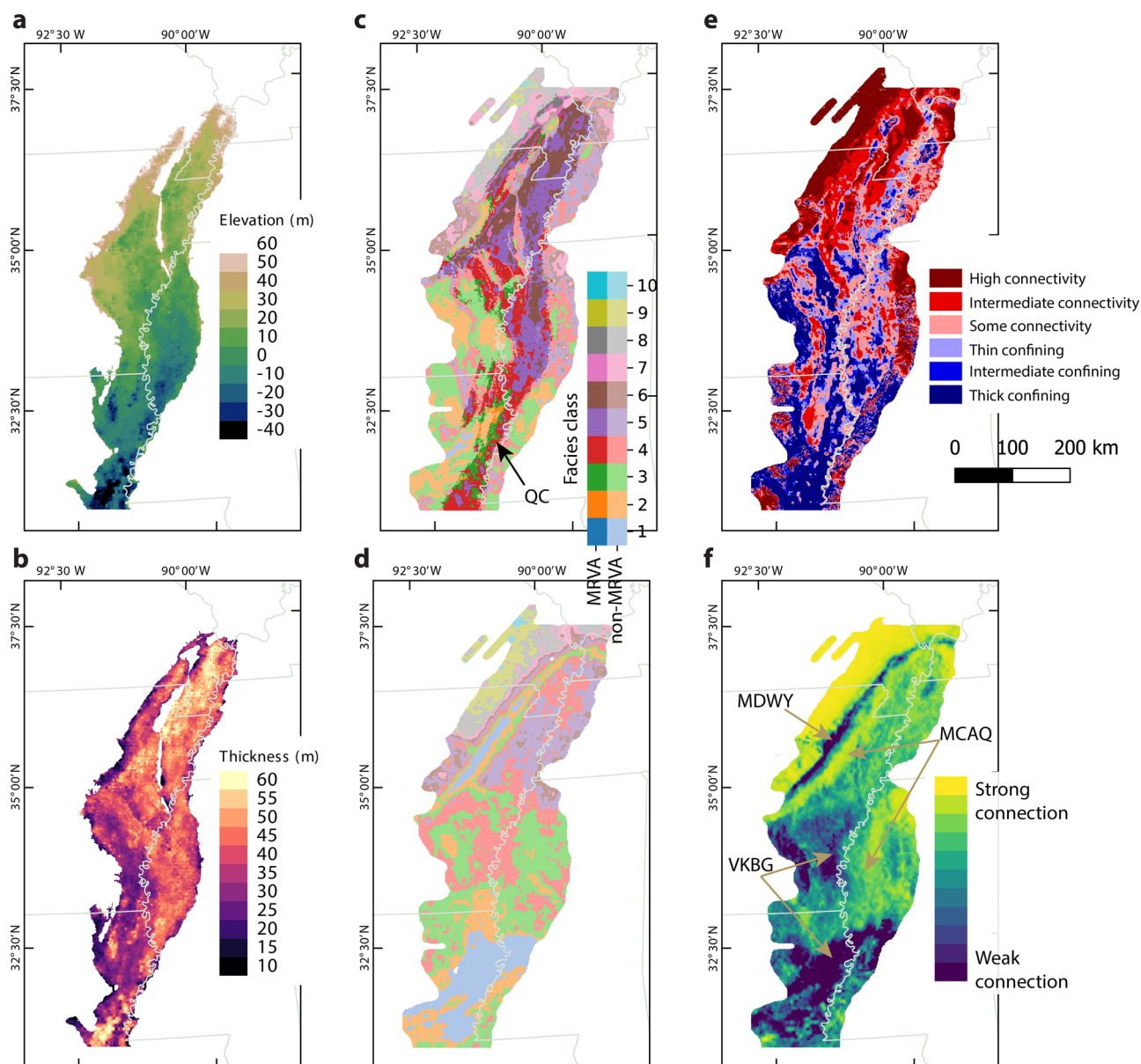


Fig. 5 Derived hydrogeologic products from AEM data. **a** Base of aquifer elevation surface determined from combined AEM and borehole data and **b** the aquifer thickness. Resistivity models grouped into facies classes at depths of 35–40 m (**c**) and 150–155 m (**d**). **e** Surficial confining and connectivity conditions based on the thickness and presence/absence of shallow low-resistivity facies classes. **f** Connectivity metric between the base of the MRVA and subcropping Tertiary unit defined as the vertically integrated electrical conductance within 25 m of the base of aquifer elevation (**a**). QC Quaternary channel, MRVA Mississippi River Valley alluvial aquifer, VKBG Vicksburg–Jackson confining unit, MCAQ Middle Claiborne aquifer, MDWY Midway confining unit.

differencing the base of aquifer elevation from the 2018 potentiometric surface, assumed here to be the water table, derived from borehole observations⁵². By subregion (Fig. 2a and Fig. S3), saturated thickness is greatest in the St. Francis region where deep Quaternary scour channels of the Mississippi–Ohio River system have been documented east of Crowleys Ridge³⁸, and thinnest in the Grand Prairie region because of the combined influence of deep water table, a thick confining layer that limits recharge, and shallow subcrop of the VKBG (Fig. 2e). The difference in saturated thickness between AEM and borehole interpretations of the base of the aquifer surface is on the order of ± 10 – 15 m (Fig. S3b). While not a large difference in absolute value, this can represent a significant percentage of aquifer thickness, which is typically < 50 m across the region. A similar approach was used to produce interpretive elevation surfaces for the top of the aquifer (bottom of surficial confining layer) and base of the aquifer for the Shellmound high-resolution study area⁵³; these surfaces were incorporated into a model-scale 3D print of the aquifer system (Fig. S4) that is being utilized as an education and outreach tool.

Building on the interpreted base of MRVA surface (Fig. 5a), we developed a continuous classification scheme throughout the entire AEM survey area intended to aid both hydrostratigraphic and geologic interpretation (Figs. 3d–f and 5c, d, “Methods” section). Numeric classes binned from low (1) to high (10) resistivity indicate groups of material expected to have similar lithology and hydraulic conductivity, thereby providing a classification with hydrostratigraphic importance. For example, where coarse-grained MRVA sediments are in direct contact with Tertiary sands of the Claiborne Group aquifers (e.g., MCAQ), resistivity values alone do not distinguish these units. As such, they may behave as a connected hydrologic unit and are therefore considered as part of the same hydrostratigraphic class. To distinguish geologic units, each class is split into two categories (MRVA or non-MRVA) based on whether or not they are within the MAP region and fall above the previously defined base of MRVA surface (Fig. 5a). In cross-section view (Fig. 3d–f) near the typical transition between the MRVA and deeper Tertiary units ~ 35 m depth (Fig. 5c), both MRVA and non-MRVA categories can be seen for the classes that span this interface where similar resistivity values are found above and below. One notable feature here includes the channel of Quaternary sediment (MRVA class 3–4) running southwest from southern Mississippi, and adjacent to the west margin of the present-day Mississippi River, which captures a subtle channel incised into the top of the more conductive VKBG (Quaternary channel, Fig. 5c). At depth, classifications generally reflect the geometry of mapped Tertiary units, with additional detail on their geometry and heterogeneity.

The permeability of surficial sediments is an important factor in parameterizing recharge for groundwater modeling⁵⁴ and in understanding aquifer vulnerability to contamination from agricultural or industrial operations⁵⁵. Here, the thickness and extent of confining material is defined by measuring the thickness of low-resistivity layers, classes 1–4 (see “Methods” section), within the uppermost 15 m (Fig. 5e). Estimates of recharge that consider soils and surficial geology layers only, without consideration of their thickness or vertical position⁵⁶, may not fully account for recharge potential. By considering the thickness of confining material, regardless of whether it is present at the land surface or buried beneath a surficial layer of more permeable material, AEM results enable a robust metric for recharge potential. For locations where low-resistivity material is absent in the near-surface, increasing potential for aquifer recharge is indicated by the average near-surface classification (Fig. 5e), with increasing classes (i.e., higher resistivity) expected to have a coarser texture and thus more connection potential between recharge and groundwater.

In addition to characterizing aquifer connectivity at the land surface (Fig. 5e), we also consider connectivity between the base of the aquifer and deeper Tertiary formations (Fig. 5f). Connectivity at the base of the aquifer is defined by considering the vertically integrated electrical conductance (vic, see “Methods” section) from 25 m above to 25 m below the base of the MRVA. Areas where the MRVA is underlain by confining Tertiary units, such as MDWY or VKBG, are characterized by low connectivity values, whereas regions of MCAQ subcrop indicate high connectivity (Fig. 5f). Between these end-members, the connectivity metric indicates a range of potential for hydrologic connection between the shallow and deep aquifer systems.

Structure and connectivity beneath rivers. Through numerous glacial cycles and concomitant changes in sea level, river networks have shaped the lower Mississippi River valley^{33,38} and are important present-day sources of aquifer recharge. To characterize the detailed subsurface structure beneath rivers, > 3000 line-km of AEM data were acquired directly along the Mississippi and Arkansas River paths, as well several smaller tributaries (Fig. 2a). For example, native-resolution, ungridded resistivity profiles with ~ 25 m spacing along flight paths for several of the tributaries (Fig. S5) illustrate similar detail as the main block flight lines in aquifer structure and geometry of the aquifer base and subcropping unit contact (Fig. S2). Following structure along the river paths enables a detailed view of the discontinuous nature of shallow confining materials beneath river systems, as well as how rivers—which are often important surface water-groundwater conduits—may be connected to the aquifer below. A persistent feature in many river profiles is the intermediate-resistivity layer at ~ 20 – 30 m depth that was more discontinuous along the main block flight lines and hypothesized earlier as a fine-grained unit separating younger and older Pleistocene sediments also indicated in Fig. S2.

In addition to streamwise surveys of river courses, gridded resistivity models from the complete regional dataset are intersected with the NHDPlus database of flowlines⁵⁷ to produce cross-sections along any river path (Fig. 6b–f). For example, flowlines intersected by the west–east flight-line block but not flown streamwise can be produced, such as the White River (Fig. 6c). Everywhere the resistivity grids intersected a stream, we use the same connectivity metric discussed previously to quantify the magnitude of connection potential between rivers and the underlying aquifer (see “Methods” section). Here, the vic connectivity metric is calculated on a version of the combined regional dataset made in 2-m depth intervals, integrated from 0 to 10 m beneath the river bottom to characterize the presence or absence of fine-grained material beneath rivers (Fig. 6a). In contrast to the MERAS model calibration for streambed conductance, which incorporated 43 streams with limited data for informing parameter values⁵⁴, the results here provide far greater coverage and finer granularity on the expected spatial patterns of streambed conductance that may be incorporated in groundwater model parameterization. To first order, surficial geology surrounding the streams³² is an important factor in the vic connectivity metric, with fine-grained units appearing less connected than coarse or intermediate units (Fig. S6).

Geological controls on groundwater age. Groundwater age can be used to assess groundwater availability by estimating recharge rates, delineating recharge areas, and characterizing aquifer susceptibility to surface contamination^{58,59}. Tritium is used to qualitatively differentiate groundwater age into modern (recharged in 1953 or later), premodern (recharged prior to

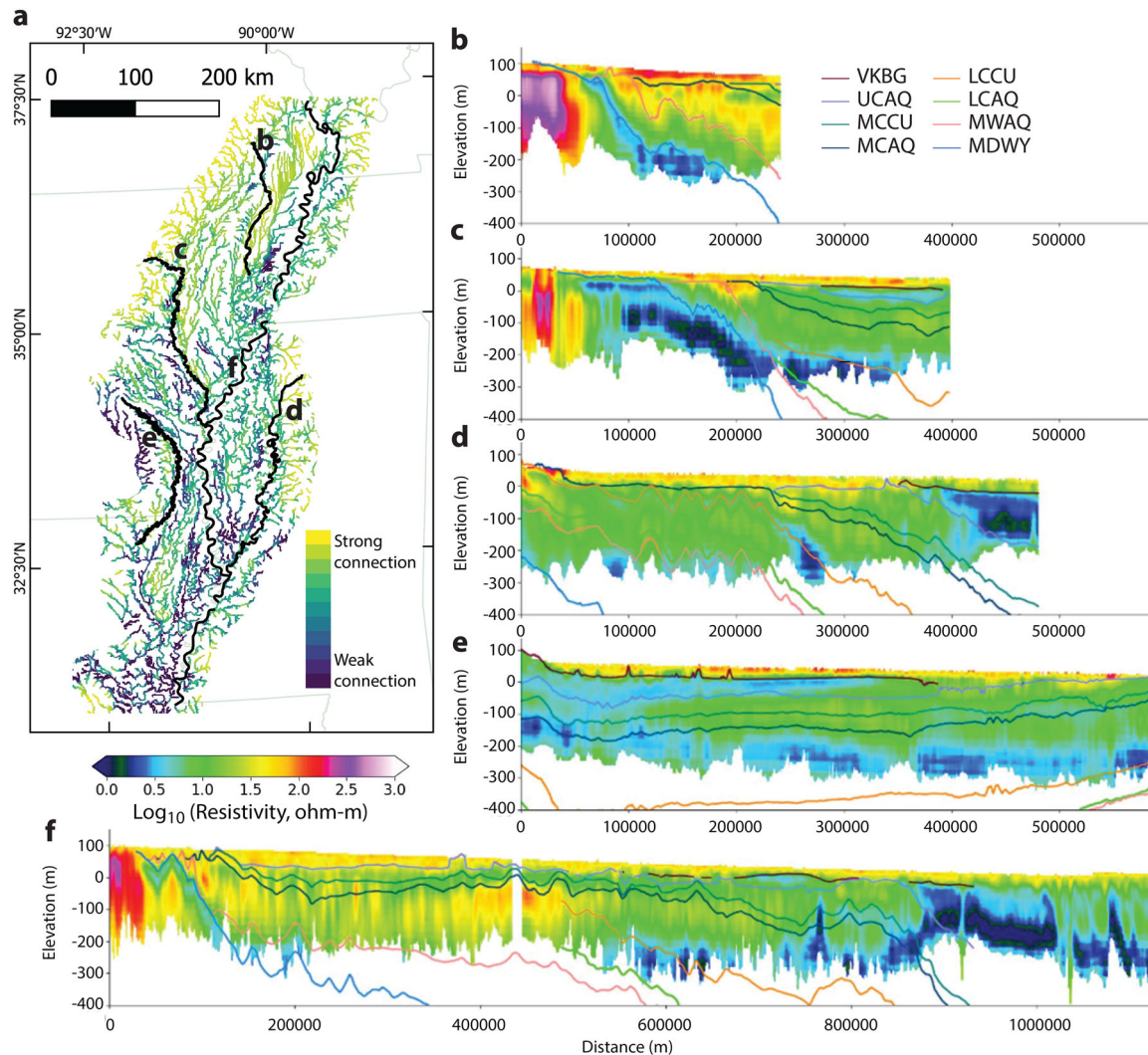


Fig. 6 Characterizing rivers and surface water-groundwater connections. **a** River connectivity metric defined along all NHDPlus segments in the study area identifies areas for high or low potential for surface water-groundwater connectivity based on streambed resistivity values. Resistivity cross-sections (from north to south) extracted from gridded data along the St. Francis River (**b**), White River (**c**), Yazoo-Tallahatchie River (**d**), Bayou Bartholomew (**e**), and Mississippi River (**f**). The top elevation of Tertiary MERAS model layers⁴³ is indicated as solid lines on top of resistivity cross-sections.

1953), or mixed (combination of modern and premodern water) groundwater categories⁶⁰. Tritium samples collected from the MAP ($n = 582$) were categorized into modern, mixed, and premodern groups⁶¹ based on the atmospheric tritium input for the well location, sample date, and the measured tritium concentration⁶⁰. Modern ages are expected for surficial alluvial aquifers in a humid region and 39.1% of MRVA samples fall in this grouping⁶¹; however, 17.9% of samples were premodern⁶¹, indicating significant variability in either recharge rates or sources of groundwater to the MRVA. The heterogeneity in MRVA groundwater age implies local-scale control, which also likely varies among the MAP regions depending on the relative importance of surface water recharge, aerial recharge through surficial confining units, or possible upwelling from deeper Tertiary units. Part of the challenge in understanding the heterogeneity of groundwater age in this system was not having regional-scale interpretations of aquifer architecture and connectivity between units.

To investigate the controls of shallow and deep connectivity on groundwater age, derivative product metrics for surface connectivity (Fig. 5e) and MRVA-Tertiary aquifer connectivity

(Fig. 5f) are plotted together with tritium age categories (Fig. 7). Samples with premodern age (Fig. 7a) have characteristically high connectivity between the MRVA and subsurface Tertiary units, along with mixed surficial connectivity, suggesting that upwelling from deeper units may control these older groundwater measurements. Conversely, both mixed and modern tritium categories show a broader range of connectivity to deeper units (Fig. 7b,c), while the modern category has the largest fraction of points (85%) that indicate some degree of surface connectivity, suggesting that connection at the surface is a controlling factor for younger samples. While further data are needed on hydrologic gradients in the system to better predict actual flow paths, these insights suggest that geological structure provides at least partial control on groundwater age and is therefore also likely to be an important driver for vertical groundwater transport. The groundwater age observations—especially the preponderance of premodern groundwater—are difficult to understand without system-scale interpretations of aquifer architecture. The finding that geological structure controls groundwater transport and age is not itself a novel concept; however, we demonstrate that system-scale AEM data can map detailed model structure that

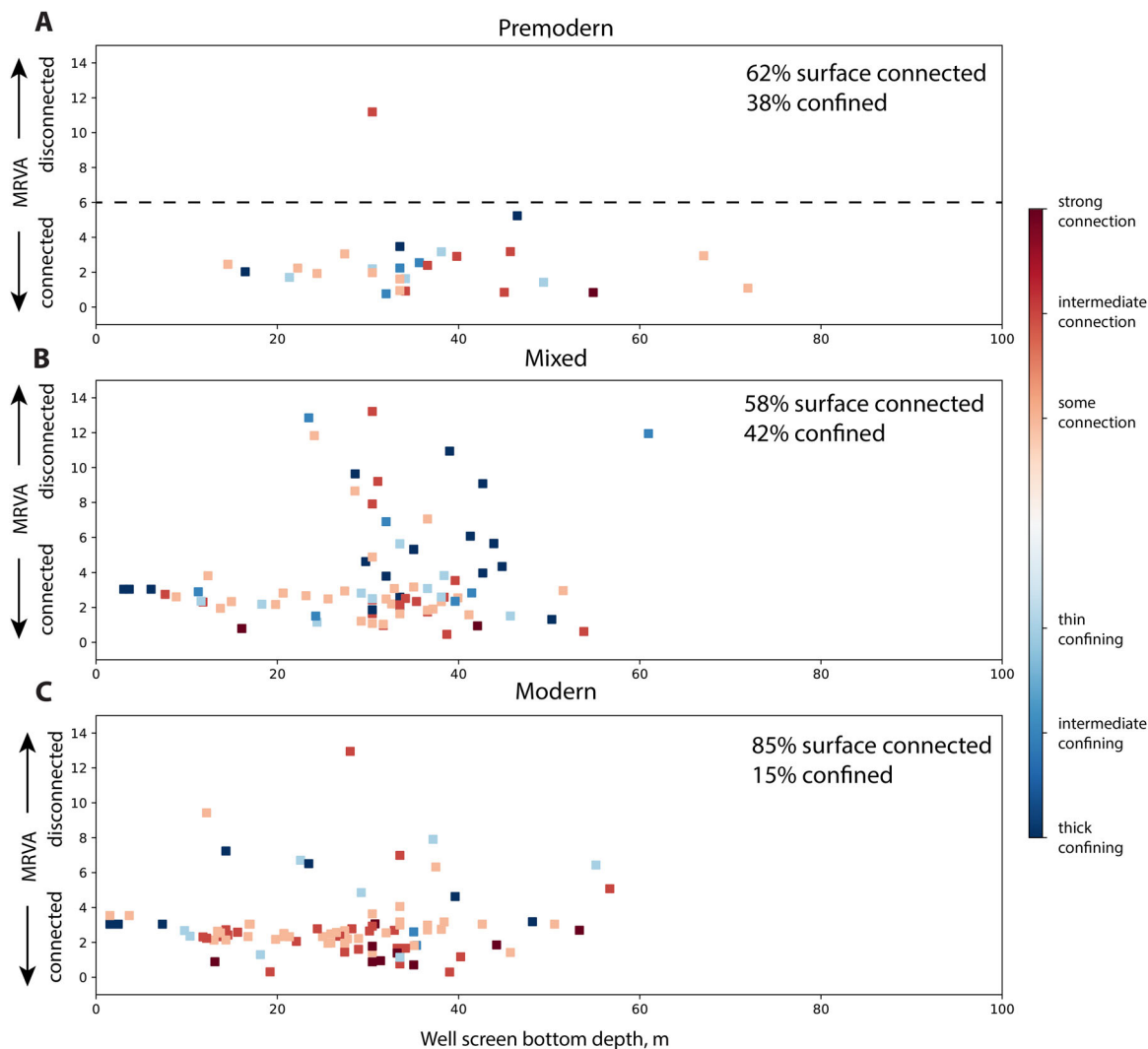


Fig. 7 Relationship between groundwater age and AEM-derived aquifer structure. Sample depth for tritium dates classified as premodern (a), mixed (b), or modern (c) is plotted against the degree of connectivity between the MRVA and deeper Tertiary units (Fig. 5f), with point colors that represent the degree of shallow aquifer connectivity (Fig. 5e).

facilitates a new understanding of hydrologic processes relevant to many applications and geologic settings.

Hidden faults along the CGL. Resistivity cross-sections west of the northeast-trending portion of Crowleys Ridge image significant up-to-the-east vertical offset—as much as ~50–75 m—that can be tracked over a distance of >100 km along two shallow fault strands (Fig. 8). These two faults closely follow the path of the ~10-km-wide CGL, just west of the RR and NMSZ⁶². The western fault splay shows a clear offset of the contact between an Upper Cretaceous high-resistivity layer at depth (McNairy Nacatosh aquifer) and the low-resistivity Tertiary MDWY within the uppermost 100–150 m (Fig. 8b–d), clearly extending to at least the base of the Quaternary aquifer. This western fault is evident on cross-sections between Fig. 8b and d (solid brown line Fig. 8a), with vertical offsets largest in the middle of this segment (up to 75 m) and maximum width ~500–1000 m. The eastern of the two faults is characterized in cross-section view by a dipping conductive layer that appears to terminate at the base of the MDWY, separating the uplifted resistive Cretaceous block to the west from the conductive MDWY to the east. Whether the dipping conductive layer is related to the MDWY or the fault

structure itself is unclear. Unlike the western fault, offset is not seen at the top of the MDWY, possibly because of Quaternary erosion of this surface. The eastern of the two structures can be traced on resistivity cross-sections over a greater distance, following the CGL to the southwest before turning south towards the Western Margin fault (Fig. 8).

While generally coincident with the CGL, both hidden faults captured in the AEM data are previously unmapped, and thus provide new insight into the tectonic history of this area. The observed uplift on these faults along the CGL can plausibly help explain the tectonic origin of Crowleys Ridge given the proximity of these features to one another. Previous geophysical and geomorphological observations along and near the ridge margins provide important insight^{63,64}—especially in relation to the eastern fault indicated here—but have not revealed the source of uplift occurring 10–20 km farther west along the CGL. Existing geophysical data along the ridge margins⁶⁴ and the CGL⁶⁵ indicate faulting and support Quaternary fault activity, but do not have sufficient spatial scale and/or resolution to delineate the discrete offset imaged by AEM data over the fault length of >100 km. The 50–75 m uplift (Fig. 8b–d) requires movement since the early Tertiary but is consistent with the Quaternary motion. The offset-wedge geometry suggests that the MDWY was lithified at

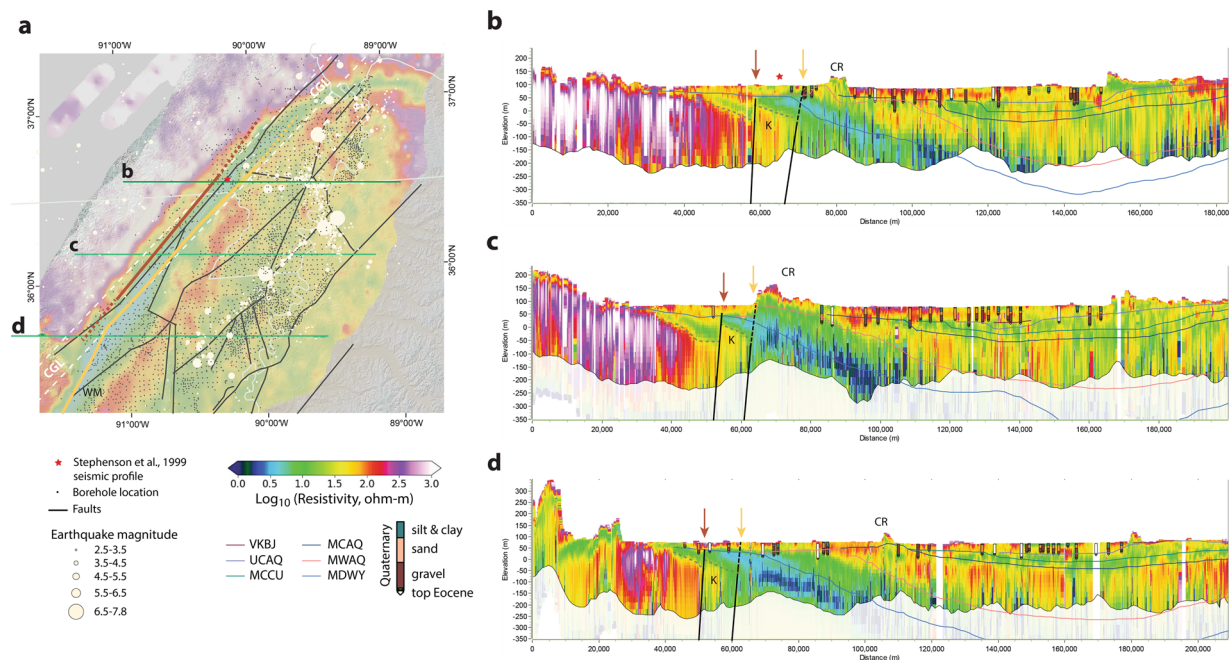


Fig. 8 Fault structures along the Commerce geophysical lineament (CGL). **a** Map view of resistivity at a depth of 60–65 m along with previously mapped fault structures and seismicity of the New Madrid seismic zone. Faults identified in this study (brown and yellow lines) fall along the 10-km-wide path of the CGL (white dashed lines)⁶². **b–d** Resistivity cross-sections indicate up to ~75 m of up-to-the-east offset on two near-vertical faults (black lines, with mapped locations marked by brown and yellow arrows) west of Crowleys Ridge, with maximum offset in the middle of the region (**c**). The western fault structure shows a clear offset of the deeper moderate-resistivity Cretaceous (K) McNairy Nacatosh aquifer against the low-resistivity Midway confining unit. The inferred base of the Midway confining unit in the vicinity of these faults is indicated by dashed lines. Location of the north–south seismic profile over the CGL⁶⁵ is indicated by a red star.

the time of deformation. Given the lack of surface expression, the majority of offset may have occurred before the 32–45 ka Melville Ridge braid belt found immediately west of Crowleys Ridge³³; however, further age constraint of Quaternary activity is not available.

Dense borehole observations that quantify the overall thickness of Quaternary sediments identify the Pliocene–Pleistocene unconformity⁴¹ and support an argument for 53 m of Quaternary uplift³⁴ in the region (Fig. 8a). However, the typical minimum separation between boreholes is >2 km and borehole density declines west of the CGL, making them also insufficient to identify this narrow fault feature as a potential source of uplift. Although the CGL and identified faults are removed from the seismically active region of the NMSZ, the possibility of Quaternary tectonic activity and offset on the faults identified here is important to understand past variations in seismicity and future hazard in the region⁶².

Multi-scale mapping. The multiple phases of AEM mapping (Fig. 2a), along with targeted ground-based⁶⁶ and waterborne⁶⁷ geophysical data collection, provide an excellent case study in the value of subsurface mapping over multiple scales. From regional surveys aggregated to 3 km line spacing with 1 km grid cells to high-resolution AEM data in the Shellmound area with 0.25–1 km line spacing with 100 m grid cells, we are able to illustrate the value of an order of magnitude increase in flight-line spacing.

The horizontal and vertical resolution of airborne geophysical surveys defines the scale of investigation, which depends on survey design parameters including instrument type, flight-line spacing, and total kilometers flown. Spatially extensive data capturing individual features several kilometers in size commensurate with mapping scales of ~1:1,000,000 (Figs. 2, 5, and 9a) are

mapped with flight-line spacing on the order of 1–10 km and effectively inform regional-scale hydrologic models and decision support. High-resolution airborne data with sub-kilometer flight-line spacing greatly improve the resolution of smaller features appropriate for local ~1:100,000-scale mapping (Fig. 9c and Fig. S7).

The high-resolution data near Shellmound, Mississippi, map coarse-grained (high-resistivity) sediments associated with river meanders that also tend to have relatively high potassium (K) abundance (Fig. S7a, b, east), in contrast with backswamp deposits and other fine-grained overbank sediments that have relatively low-resistivity and greater thorium (Th) abundance. At 50–55 m depth (Fig. 9c and Fig. S7d), resistivity models map a buried paleochannel in the southeast corner of the grid that appears incised to depths of at least 75 m. This channel was previously unknown and may be a relict of the ancestral Mississippi–Ohio river system that flowed east of Crowleys Ridge during the Pleistocene³³, creating conduits for local groundwater flow. Deep channels such as this are likely present throughout the region, but are under-sampled by borehole observations and even the regional geophysical flight lines (Figs. 2d–h, 3a–c).

The combination of spatially extensive and high-resolution data enables detection and mapping of small-scale or hidden features that would otherwise be missed (i.e., the known unknowns in the subsurface). Our results demonstrate the value in AEM for imaging localized pathways for groundwater connection above and below the aquifer (Fig. 5e, f), buried paleochannels (Fig. 9c), and hidden faults with narrow zones of uplift previously unmapped (Fig. 8). These discrete and relatively small features may have an outsized and nonlinear impact on model predictions, hazard assessments, and decision making, but are impossible to recognize with sparse or limited spatial coverage.

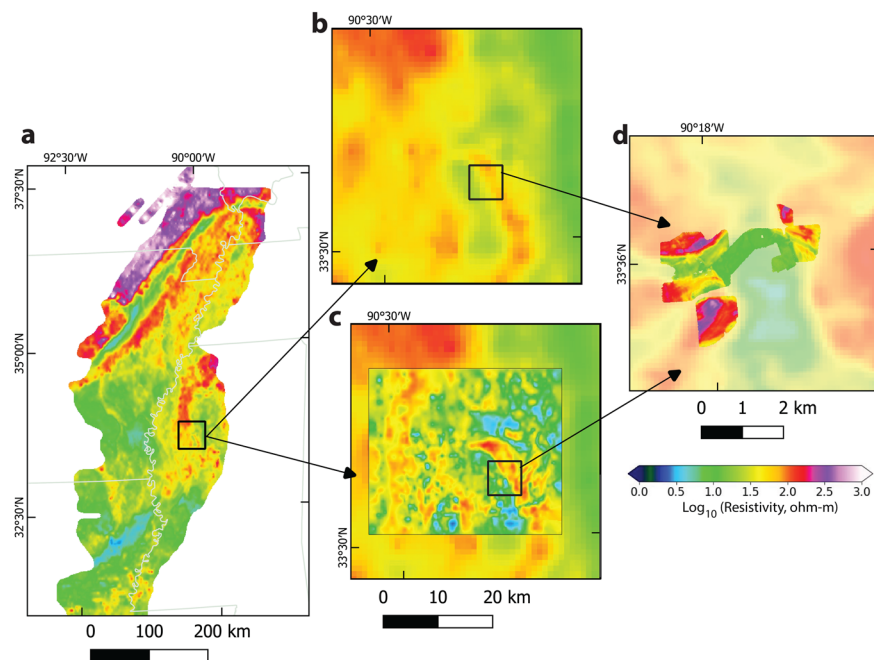


Fig. 9 Multi-scale mapping with airborne and ground-based methods. **a** Regional-scale structure mapped on 1 km grid cells interpolated from ~3 to 6 km-spaced flight-line data over the entire MAP region. **b** Regional-scale structure enlarged to the ~30 × 30 km Shellmound study area, compared with high-resolution structure mapped on 100 m grid cells interpolated from 0.25 to 1 km-spaced flight-line data from the Shellmound study area (**c**) shows the ability to resolve detailed buried channel structure. **d** Comparison of near-surface high-resolution Shellmound AEM data (background) with very high-resolution ground-based electromagnetic data⁶⁶ acquired with a sensor towed over ~4 km² on survey lines spaced by 25 m.

Outlook and future directions. An emerging example of “big data” in geoscience, AEM is expanding the breadth of information that can be applied to near-surface investigation and modeling where detail about subsurface complexity is lacking. Many process-based hydrologic models have evolved to function in the absence of detailed subsurface structural information, largely because these data are typically not available and because incorrect assumptions about subsurface structure and unwarranted complexity lead to modeling errors⁶⁸. Technological advances in remote sensing and airborne geophysics present new opportunities to advance the level of geological detail that can be incorporated in hydrologic models through the entire vertical extent of an aquifer system. As “big data” have become available to constrain details of model structure, commensurate advances in modeling, such as machine learning and uncertainty quantification⁶⁹, will also be needed to realize the full potential of airborne geophysical datasets.

As the dimension and complexity of questions that may be asked of a model or array of models (i.e., the “decision-space”) continue to increase, the need for detailed data to support these questions also increases. When allocating resources for data collection, a balance should be sought between the optimality of data collection to address a narrow decision-space (such as a single, focused question) and robustness of the investment to address future questions that expand the decision-space. The variety of applications demonstrated in this study highlights the robustness of large-scale AEM data in this respect. Although AEM surveys can involve high absolute cost, at large scales they may be 3–4 orders of magnitude less expensive on a per-data-point or per-square-kilometer basis compared with traditional ground-based surveys or drilling. Because large surveys can cover parts of multiple counties and states and support the interests of multiple scientific disciplines or stakeholder interests, a community-driven approach to the acquisition of these foundational geoscientific datasets is advantageous. Benefits of a

coordinated approach to acquiring system-scale AEM data include reduced costs to individual participants, leveraging resources to acquire more data than any individual group could achieve, and ensuring data consistency across the study area that maximizes their value.

Much as lidar has transformed our understanding of Earth’s surface, airborne geophysical data extend our view into the subsurface, transforming our ability to inform three-dimensional mapping from catchment to basin scales (Fig. 1b). Here, we demonstrated that system-scale AEM data provide a robust platform from which to address a host of subsurface questions. Airborne geophysical datasets represent the next generation in subsurface mapping, capable of filling in the gaps between existing boreholes with an order of magnitude or greater increase in data density. This will provide nationally consistent near-surface geologic datasets as a foundation for three-dimensional geologic interpretations, hydrologic models, and other subsurface studies that rely on detailed measurements of difficult to access belowground properties within 200–300 m of Earth’s surface (i.e., lidar for the subsurface).

Methods

Airborne data collection. Airborne geophysical data were acquired in three phases through a competitive award to CGG Airborne, using two different AEM platforms that also included magnetic and radiometric sensors: (Phase 1) A high-resolution grid with flight-line spacing between 0.25 and 1 km covered an area of ~1000 km² just northwest of Shellmound, Mississippi. (Phase 2) A regional grid covered over 95,000 km² with 6–12 km between flight lines over most of the area, plus an area of higher density (1.5 km line spacing) over part of southern Crowley’s Ridge in Arkansas. This regional survey also included ~2000 line-km of data acquired directly along several streams and rivers to characterize their potential for enhancing connectivity between surface water and groundwater. (Phase 3) A second regional survey extended coverage to an area of ~140,000 km² with 6 km between flight lines, interwoven with the first regional grid such that the combined line spacing was 3 km over most of the study area. An additional 1400 line-km were acquired streamwise along the entire Mississippi River within the study area, as well as the Arkansas River from Little

Rock, Arkansas, to its confluence with the Mississippi River. The first two phases of data collection were acquired with the helicopter-based Resolve frequency-domain AEM system, while the third phase was acquired with the fixed-wing time-domain Tempest AEM system.

The Resolve AEM system was flown in the first two phases (Fig. 2a), first in March 2018 for a high-resolution study near Shellmound, Mississippi^{53,70}, and again in the regional mapping effort from November 2018 to February 2019 that covered most of the MAP study area⁷¹. The Resolve AEM system is a frequency-domain electromagnetic sensor that operates with six independent transmitter–receiver coil pairs at discrete frequencies from 400 to 140,000 Hz¹⁸. Five of the coil pairs are oriented in a horizontal coplanar configuration (horizontal coils with vertical magnetic dipole) and separated by 7.9 m, with one coil pair in a vertical coaxial configuration (vertical coils with horizontal magnetic dipole in the flight direction) separated by 9.1 m. Data are recorded at a 10-Hz sampling interval with nominal flight speed 130 km/h and instrument height 30 m above the terrain. The Resolve instrument is slung ~30 m beneath a Eurocopter AS350 B2 helicopter. The typical depth of investigation for the Resolve system is 60–100 m, with high vertical resolution in the uppermost 2–5 m below land surface.

The Tempest AEM system was flown in the third phase of surveys, covering the entire study area (Fig. 2a) from November 2019 to March 2020⁷². Tempest is a time-domain electromagnetic sensor⁷³ acquired from a fixed-wing platform (Cessna 208B), with a transmitter loop attached to the airframe and a three-component receiver coil in a bird that is towed behind the aircraft. The Tempest transmitter is a horizontal loop with an area 155 m² and an average moment 43,400 Am². The three-component receiver is towed nominally 108 m behind and 50 m below the transmitter, with actual position during flight recorded by GPS. Inertial measurement unit sensors are mounted in the aircraft and the receiver bird measured transmitter and receiver orientation, respectively. Recorded dB/dt data for each channel are transformed to B-field responses that would be observed for a perfect 100% duty cycle transmitter waveform⁷³, and are provided in 15 channels with window center times from 11 to 13,400 μ s. Data are recorded at a 5 Hz sampling interval with a nominal flight speed of 200 km/h and a flying height of 120 m above the terrain. The typical depth of investigation for the Tempest system is 200–300 m, with moderate vertical resolution in the uppermost 5–10 m below land surface.

Complete details of system and acquisition parameters for each survey phase can be found in the contractor-provided reports^{70–72}.

Inversion of AEM data and combined geophysical products. Resolve AEM data were inverted to recover subsurface electrical resistivity structure using the Aarhus Workbench software (Aarhus GeoSoftware, Aarhus, Denmark) that builds on the AarhusInv code⁷⁴. Input data included 12 data channels of in-phase and quadrature measurements from each of the six coil pairs, along with laser altimeter measurements of the instrument height above ground. Data were manually edited to remove noisy measurements caused by manmade infrastructure before inversion. Inverted resistivity models were estimated on a 30-layer structure from depths of 1–125 m below ground, and models were output approximately every 25 m along flight lines. A laterally constrained inversion process added lateral constraints between neighboring models to promote spatial continuity across models. In addition to resistivity values, the algorithm also produced estimates of transmitter height above ground, parameter uncertainty, and depth of investigation⁷⁵. Data and inverted model results are available in the online ScienceBase repository^{70,71}.

Tempest AEM data were inverted to recover subsurface electrical resistivity structure using the GALEI code developed by Geoscience Australia, including specific functionality for the Tempest system⁷⁶. Input data included 30 data channels of delivered B-field observations for both x- and z-component receiver coils (15 channels each). System geometry included transmitter altitude and attitude, as well as transmitter–receiver offset and receiver attitude, all of which were input into the inversion. Inverted resistivity models were estimated on a 30-layer structure from depths of 4–400 m below ground, and models were output approximately every 75 m along flight lines. In addition to resistivity values, the algorithm also produced estimates of transmitter height above ground, parameter uncertainty, and depth of investigation⁷⁵. Data and inverted model results are available in the online ScienceBase repository⁷².

We combined the Resolve and Tempest resistivity models in three steps. First, for each dataset, resistivity models were discretized onto a common 1 km resolution grid⁴⁵ for 5 m depth intervals, including model values down to the estimated depth of investigation for each grid point. Second, we kriged each dataset using the geostatspy library (<https://github.com/GeostatsGuy/GeostatsPy>) that incorporates GSLIB functions⁷⁷, using empirical semivariograms to define the correlation structure for each layer. Lastly, the Resolve and Tempest kriged grids for each depth interval were combined using a weighted function that smoothly transitioned from a mix of 0.52/0.48 Resolve/Tempest in the shallowest layer to 0.00/1.00 Resolve/Tempest by a depth of 75 m⁷⁸.

Derivative products

Base aquifer. The elevation of the base of the MRVA was determined using a supervised machine learning algorithm⁵¹ that uses 6130 existing borehole picks³⁹ along with 364 additional manual picks and AEM-derived resistivity data, as

Table 1 Resistivity classification thresholds.

Class no.	Resistivity, ohm-m
1	<3.16
2	3.16–6.49
3	6.49–13.34
4	13.34–27.38
5	27.38–56.23
6	56.23–115.48
7	115.48–237.14
8	237.14–486.97
9	486.97–1000.00
10	>1000.00

training. Based on these inputs, the algorithm predicts the base of MRVA elevation at all AEM data locations, with values interpolated to a regular grid with 1 km spatial resolution⁷⁹.

Facies classification. The kriged resistivity grids described above were categorized into ten classes (Table 1) intended to group materials expected to have similar hydrologic and geologic properties based on their resistivity. In some cases, different juxtaposed geologic materials may have similar lithology, such as MRVA sands that overlie coarse-grained Tertiary sands, which cannot be distinguished based on their resistivity alone, and may, in fact, behave as a connected hydrostratigraphic unit. To provide additional geological interpretation, we also classified resistivity grids based on their position relative to the base of MRVA surface discussed above. For example, similar resistivity values above and below the base of MRVA surface would belong to the same class number, but are separated into MRVA and non-MRVA groups based on their vertical position. In this fashion, our classification system includes both hydrostratigraphic and geologic information. The non-MRVA class captures both Tertiary units beneath the MRVA and rocks and sediments outside the footprint of the MAP region, including Crowley's Ridge. Resistivity thresholds that separate the classes are chosen on a uniform logarithmic spacing between reasonable minimum and maximum values observed in the dataset. Classes qualitatively correspond with known lithologic transitions discussed above; however, sufficient data are not available to produce a quantitative calibration of class groupings against borehole and other geologic or hydrologic datasets for the entire region (Table 1).

Connectivity. We defined a vertically integrated connectivity metric as the vic across an interval of interest:

$$\text{vic} = \sum_{i=1}^n \frac{t_i}{\rho_i}$$

For each layer (i) within an interval, the electrical conductance is defined as the product of layer thickness (t_i) and the inverse of the layer resistivity (ρ_i). The vic is the sum of layer conductances and is intended to highlight the presence and thickness of low-resistivity material that may be a barrier to vertical hydrologic connectivity across the interval.

Data availability

Geophysical data and derived products are available at the USGS ScienceBase repository: <https://www.sciencebase.gov/catalog/item/5e8dd9882cee42d13468786>.

Received: 9 February 2021; Accepted: 28 May 2021;

Published online: 22 June 2021

References

- Siebert, S. et al. Groundwater use for irrigation – a global inventory. *Hydrol. Earth Syst. Sci.* **14**, 1863–1880 (2010).
- Margat, J. & van der Gun, J. *Groundwater Around the World: A Geographic Synopsis* (CRC Press/Balkema, 2013).
- WWAP (United Nations World Water Assessment Programme). *The United Nations World Water Development Report 2015: Water for a Sustainable World* (WWAP, 2015).
- Rodell, M. et al. Emerging trends in global freshwater availability. *Nature* **557**, 651–659 (2018).
- Famiglietti, J. S. The global groundwater crisis. *Nat. Clim. Change* **4**, 945–948 (2014).
- Alley, W. M., Healy, R. W., LaBaugh, J. W. & Reilly, T. E. Flow and storage in groundwater systems. *Science* **296**, 1985–1990 (2002).

7. Lovelace, J. K., Nielsen, M. G., Read, A. L., Murphy, C. J. & Maupin, M. A. Estimated groundwater withdrawals from principal aquifers in the United States, 2015. *US Geol. Surv. Circ.* **1464**, 82 (2020).
8. Dieter, C. A. et al. Estimated use of water in the United States in 2015. *US Geol. Surv. Circ.* **1441**, 76 (2018).
9. Clark, B. R., Hart, R. M. & Gurdak, J. J. Groundwater availability of the Mississippi Embayment. *US Geol. Surv. Prof. Pap.* **1785**, 62 (2011).
10. USDA National Agricultural Statistics Service. 2017 Census of agriculture. www.nass.usda.gov/AgCensus (2019).
11. Alhassan, M., Lawrence, C. B., Richardson, S. & Pindilli, E. J. The Mississippi Alluvial Plain aquifers—an engine for economic activity. *US Geol. Surv. Fact Sheet* <https://doi.org/10.3133/fs20193003> (2019).
12. Becker, M. W. Potential for satellite remote sensing of ground water. *Groundwater* **44**, 306–318 (2006).
13. Rodell, M. & Famiglietti, J. S. The potential for satellite-based monitoring of groundwater storage changes using GRACE: the High Plains aquifer, Central US. *J. Hydrol.* **263**, 245–256 (2002).
14. Galloway, D. L. et al. Detection of aquifer system compaction and land subsidence using interferometric synthetic aperture radar, Antelope Valley, Mojave Desert, California. *Water Resour. Res.* **34**, 2573–2585 (1998).
15. Entekhabi, D. et al. The soil moisture active passive (SMAP) mission. *Proc. IEEE* **98**, 704–716 (2010).
16. National Academies of Sciences, Engineering, and Medicine. *Groundwater Recharge and Flow: Approaches and Challenges for Monitoring and Modeling Using Remotely Sensed Data: Proceedings of a Workshop* (The National Academies Press, 2019).
17. Fitterman, D. V. & Deszcz-Pan, M. Helicopter EM mapping of saltwater intrusion in Everglades National Park, Florida. *Explor. Geophys.* **29**, 240–243 (1998).
18. Siemon, B., Christiansen, A. V. & Auken, E. A review of helicopter-borne electromagnetic methods for groundwater exploration. *Near Surface Geophys.* **7**, 629–646 (2009).
19. Viezzoli, A., Tosi, L., Teatini, P. & Silvestri, S. Surface water-groundwater exchange in transitional coastal environments by airborne electromagnetics: the Venice Lagoon example. *Geophys. Res. Lett.* **37**, L01402 (2010).
20. Auken, E., Boesen, T. & Christiansen, A. V. in *Advances in Geophysics*, Vol. 58 (ed. Nielsen, L.), 47–93 (Elsevier, 2017).
21. Korus, J. T., Joeckel, R. M., Divine, D. P. & Abraham, J. D. Three-dimensional architecture and hydrostratigraphy of cross-cutting buried valleys using airborne electromagnetics, glaciated Central Lowlands, Nebraska, USA. *Sedimentology* **64**, 553–581 (2017).
22. Knight, R. et al. Mapping aquifer systems with airborne electromagnetics in the Central Valley of California. *Groundwater* **56**, 893–908 (2018).
23. Chandra, S., Auken, E., Maurya, P. K., Ahmed, S. & Verma, S. K. Large scale mapping of fractures and groundwater pathways in crystalline hardrock by AEM. *Sci. Rep.* **9**, 398 (2019).
24. Ball, L. B., Davis, T. A., Minsley, B. J., Gillespie, J. M. & Landon, M. K. Probabilistic categorical groundwater salinity mapping from airborne electromagnetic data adjacent to California's Lost Hills and Belridge oil fields. *Water Resour. Res.* **56**, e2019WR026273 (2020).
25. Minsley, B. J. et al. Airborne electromagnetic imaging of discontinuous permafrost. *Geophys. Res. Lett.* **39**, L02503 (2012).
26. Mikucki, J. A. et al. Deep groundwater and potential subsurface habitats beneath an Antarctic dry valley. *Nat Commun.* **6**, 6831 (2015).
27. Walter Anthony, K. et al. 21st-century modeled permafrost carbon emissions accelerated by abrupt thaw beneath lakes. *Nat. Commun.* **9**, 3262 (2018).
28. Christensen, C., Pfaffhuber, A. A., Anshütz, H. & Smaavik, T. F. Combining airborne electromagnetic and geotechnical data for automated depth to bedrock tracking. *J. Appl. Geophys.* **119**, 178–191 (2015).
29. Finn, C. A., Sisson, T. W. & Deszcz-Pan, M. Aerogeophysical measurements of collapse-prone hydrothermally altered zones at Mount Rainier volcano. *Nature* **409**, 600 (2001).
30. Finn, C. A., Deszcz-Pan, M., Ball, J. L., Bloss, B. J. & Minsley, B. J. Three-dimensional geophysical mapping of shallow water saturated altered rocks at Mount Baker, Washington: Implications for slope stability. *J. Volcanol. Geotherm. Res.* **357**, 261–275 (2018).
31. Fisk, H. N. *Geological Investigation of the Alluvial Valley of the Lower Mississippi River*, 78 (Mississippi River Commission, 1944).
32. Saucier, R. T. *Geomorphology and Quaternary Geologic History of the Lower Mississippi Valley* (US Army Engineer Waterways Experiment Station, 1994).
33. Rittenour, T. M., Blum, M. D. & Goble, R. J. Fluvial evolution of the lower Mississippi River valley during the last 100 k.y. glacial cycle: response to glaciation and sea-level change. *GSA Bull.* **119**, 586–608 (2007).
34. Van Arsdale, R. B., Cox, R. T. & Lumsden, D. N. Quaternary uplift in the Lower Mississippi River Valley. *J. Geol.* **127**, 000–000 (2018).
35. Cox, R. T. & Van Arsdale, R. B. The Mississippi Embayment, North America: a first order continental structure generated by the Cretaceous superplume mantle event. *J. Geodyn.* **34**, 163–176 (2002).
36. Cushing, E. M., Boswell, E. H. & Hosman, R. L. General geology of the Mississippi embayment. *US Geol. Surv. Prof. Pap.* <https://doi.org/10.3133/pp448B> (1964).
37. Odom, W., Hofmann, F., Van Arsdale, R. & Granger, D. New 26Al/10Be and (U-Th)/He constraints on the age of the Upland Complex, central Mississippi River Valley. *Geomorphology* **371**, 107448 (2020).
38. Van Arsdale, R. B., Cupples, W. B. & Csontos, R. M. Pleistocene–Holocene transition in the central Mississippi River valley. *Geomorphology* **214**, 270–282 (2014).
39. Torak, L. J. & Painter, J. A. Geostatistical estimation of the bottom altitude and thickness of the Mississippi River Valley alluvial aquifer. *US Geol. Surv. Scientific Investig. Map* **3426**, 2 (2019).
40. Shen, Z. et al. Rapid and widespread response of the Lower Mississippi River to eustatic forcing during the last glacial-interglacial cycle. *GSA Bull.* **124**, 690–704 (2012).
41. Csontos, R., Arsdale, R. V., Cox, R. & Waldron, B. Reelfoot rift and its impact on Quaternary deformation in the central Mississippi River valley. *Geosphere* **4**, 145–158 (2008).
42. Calais, E., Freed, A. M., Van Arsdale, R. & Stein, S. Triggering of new Madrid seismicity by late-Pleistocene erosion. *Nature* **466**, 608–611 (2010).
43. Hart, R. M., Clark, B. R. & Bolyard, S. E. Digital surfaces and thicknesses of selected hydrogeologic units within the Mississippi Embayment Regional Aquifer Study (MERAS). *US Geol. Surv. Sci. Investig. Rep.* <https://doi.org/10.3133/sir20085098> (2008).
44. Hart, R. M. & Clark, B. R. Geophysical log database for the Mississippi Embayment Regional Aquifer Study (MERAS). *US Geol. Surv. Sci. Investig. Rep.* <https://doi.org/10.3133/sir20085192> (2008).
45. Langenheim, V. E. & Hildenbrand, T. G. Commerce geophysical lineament—its source, geometry, and relation to the Reelfoot rift and New Madrid seismic zone. *GSA Bull.* **109**, 580–595 (1997).
46. Hildenbrand, T. G. Rift structure of the northern Mississippi Embayment from the analysis of gravity and magnetic data. *J. Geophys. Res.* **90**, 12607–12622 (1985).
47. Kingsbury, J. A. et al. The quality of our Nation's waters: water quality in the Mississippi embayment-Texas coastal uplands aquifer system and Mississippi River Valley alluvial aquifer, south-central United States, 1994–2008. *US Geol. Surv. Circ.* **1356**, 84 (2015).
48. Knierim, K. J., Kingsbury, J. A., Haugh, C. J. & Ransom, K. M. Using boosted regression tree models to predict salinity in Mississippi Embayment aquifers, central United States. *J. Am. Water Resour. Assoc.* <https://doi.org/10.1111/1752-1688.12879> (2020).
49. Archie, G. E. The electrical resistivity log as an aid in determining some reservoir characteristics. *Trans. Am. Inst. Min. Metall. Pet. Eng.* **146**, 54–62 (1942).
50. Waxman, M. H. & Smits, L. J. M. Electrical conductivities in oil-bearing shaly sands. *Soc. Pet. Eng. J.* **8**, 107–122 (1968).
51. Gulbrandsen, M., Ball, L., Minsley, B. & Hansen, T. Automatic mapping of the base of aquifer—a case study from Morrill, Nebraska. *Interpretation* **5**, T231–T241 (2017).
52. McGuire, V. L. et al. Altitude of the potentiometric surface in the Mississippi River Valley alluvial aquifer, spring 2018. *US Geol. Surv. Sci. Investig. Map* **3453**, 22 (2020).
53. Burton, B. L. et al. High-resolution airborne geophysical survey of the Shellmound, Mississippi area. *US Geol. Survey Sci. Investig. Map* 3449, <https://doi.org/10.3133/sim3449> (2020).
54. Clark, B. R. & Hart, R. M. The Mississippi Embayment Regional Aquifer Study (MERAS): documentation of a groundwater-flow model constructed to assess water availability in the Mississippi embayment. *US Geol. Surv. Sci. Investig. Rep.* <https://doi.org/10.3133/sir20095172> (2009).
55. Gonthier, G. & Mahon, G. L. Thickness of the Mississippi River Valley confining unit, eastern Arkansas. *US Geol. Surv. Water Resour. Investig. Rep.* <https://doi.org/10.3133/wri924121> (1993).
56. Reitz, M., Sanford, W. E., Senay, G. B. & Cazenias, J. Annual estimates of recharge, quick-flow runoff, and evapotranspiration for the contiguous US using empirical regression equations. *J. Am. Water Resour. Assoc.* **53**, 961–983 (2017).
57. McKay, L. et al. *NHDPlus Version 2: User Guide (Data Model Version 2.1)* (US Environmental Protection Agency, 2012).
58. McMahon, P. B., Plummer, L. N., Böhlke, J. K., Shapiro, S. D. & Hinkle, S. R. A comparison of recharge rates in aquifers of the United States based on groundwater-age data. *Hydrogeol. J.* **19**, 779–800 (2011).
59. Kingsbury, J. A., Barlow, J. R. B., Jurgens, B. C., McMahon, P. B. & Carmichael, J. K. Fraction of young water as an indicator of aquifer vulnerability along two regional flow paths in the Mississippi embayment aquifer system, southeastern USA. *Hydrogeol. J.* **25**, 1661–1678 (2017).
60. Lindsey, B. D., Jurgens, B. C. & Belitz, K. Tritium as an indicator of modern, mixed, and premodern groundwater age. *US Geol. Surv. Sci. Investig. Rep.* <https://doi.org/10.3133/sir20195090> (2019).

61. Wacaster, S. R., Gratzner, M. C., Knierim, K. J. & Kingsbury, J. A. Tritium age categories of groundwater from the Mississippi River Valley alluvial aquifer and aquifers of the Mississippi embayment principal aquifer system. *US Geol. Surv. Data Rel.* <https://doi.org/10.5066/P9980P5H> (2020).
62. Baldwin, J. N. et al. Geological characterization of the Idalia Hill fault zone and its structural association with the Commerce geophysical lineament, Idalia, Missouri. *Bull. Seismol. Soc. Am.* **96**, 2281–2303 (2006).
63. Thompson Jobe, J. A. et al. Evidence for late Quaternary deformation along Crowley's Ridge, New Madrid seismic zone. *Tectonics* **39**, e2019TC005746 (2020).
64. Van Arsdale, R. B. et al. The origin of Crowley's Ridge, northeastern Arkansas: erosional remnant or tectonic uplift? *Bull. Seismol. Soc. Am.* **85**, 963–985 (1995).
65. Stephenson, W. J. et al. Deformation and Quaternary faulting in southeast Missouri across the Commerce geophysical lineament. *Bull. Seismol. Soc. Am.* **89**, 140–155 (1999).
66. Pace, M. D. M., Minsley, B. J. & Moulton, C. W. Ground-based electromagnetic survey, Shellmound, Mississippi, October 2018. *US Geol. Surv. Data Rel.* <https://doi.org/10.5066/P9YRT884> (2020).
67. Lane, J. W. et al. Characterizing the diverse hydrogeology underlying rivers and estuaries using new floating transient electromagnetic methodology. *Sci. Total Environ.* **740**, 140074 (2020).
68. Hunt, R. J., Doherty, J. & Tonkin, M. J. Are models too simple? Arguments for increased parameterization. *Groundwater* **45**, 254–262 (2007).
69. Minsley, B. J., Foks, N. L. & Bedrosian, P. A. Quantifying model structural uncertainty using airborne electromagnetic data. *Geophys. J. Int.* <https://doi.org/10.1093/gji/ggaa393> (2020).
70. Burton, B. L. et al. Airborne electromagnetic, magnetic, and radiometric survey, Shellmound, Mississippi, March 2018. *US Geol. Surv. Data Rel.* <https://doi.org/10.5066/P9D4EA9W> (2019).
71. Burton, B. L., Minsley, B. J., Bloss, B. R. & Kress, W. H. Airborne electromagnetic, magnetic, and radiometric survey of the Mississippi Alluvial Plain, November 2018 – February 2019. *US Geol. Surv. Data Rel.* <https://doi.org/10.5066/P9XBBUU> (2021).
72. Minsley, B. J. et al. Airborne electromagnetic, magnetic, and radiometric survey of the Mississippi Alluvial Plain, November 2019 – March 2020. *US Geol. Surv. Data Rel.* <https://doi.org/10.5066/P9E44CTQ> (2021).
73. Lane, R. et al. An example of 3D conductivity mapping using the TEMPEST airborne electromagnetic system. *Explor. Geophys.* **31**, 162–172 (2000).
74. Auken, E. et al. An overview of a highly versatile forward and stable inverse algorithm for airborne, ground-based and borehole electromagnetic and electric data. *Explor. Geophys.* **46**, 223–235 (2015).
75. Christiansen, A. V. & Auken, E. A global measure for depth of investigation. *Geophysics* **77**, WB171–WB177 (2012).
76. Brodie, R. *ga-aem: Modelling and Inversion of Airborne Electromagnetic (AEM) Data in 1D* (Geoscience Australia, 2017).
77. Deutsch, C. V. & Journel, A. G. *GSLIB: Geostatistical Software Library and User's Guide* (Oxford Univ. Press, 1997).
78. James, S. R. & Minsley, B. J. Combined results and derivative products of hydrogeologic structure and properties from airborne electromagnetic surveys in the Mississippi Alluvial Plain. *US Geol. Surv. Data Rel.* <https://doi.org/10.5066/P9382RCI> (2021).
79. Clark, B. R. et al. National-scale grid to support regional groundwater availability studies and a national hydrogeologic database. *US Geol. Surv. Data Rel.* <https://doi.org/10.5066/F7P84B24> (2018).

Acknowledgements

This study was funded by the US Geological Survey (USGS) MAP project, as a federal appropriation to the USGS Water Availability and Use Science Program. Airborne geophysical data were acquired by CGG Airborne through a competitive open solicitation. We are grateful for helpful comments that improved the manuscript from Jesse Korus, Randy Cox, Rosemary Knight, and Carole Johnson. Any use of trade, firm, or product names is for descriptive purposes only and does not imply endorsement by the US Government.

Author contributions

B.J.M. oversaw all aspects of the airborne geophysical surveys, data analysis, and interpretation, and led to the development of the paper. J.R.R. and W.H.K. led the overall MAP project and were central to planning and execution of the airborne geophysical surveys along with the interpretation of results and integration with the larger project team. S.R.J., B.L.B., P.A.B., and M.D.M.P. contributed to various aspects of airborne survey processing, analysis, and interpretation. S.R.J. produced most of the content in the derivative product and river figures. K.J.K. led analysis of the groundwater salinity data and tritium dating and contributed to their integration with geophysical results. All authors contributed to writing the paper.

Competing interests

The authors declare no competing interests.

Additional information

Supplementary information The online version contains supplementary material available at <https://doi.org/10.1038/s43247-021-00200-z>.

Correspondence and requests for materials should be addressed to B.J.M.

Peer review information Communications Earth & Environment thanks the anonymous reviewers for their contribution to the peer review of this work. Primary Handling Editor: Joe Aslin

Reprints and permission information is available at <http://www.nature.com/reprints>

Publisher's note Springer Nature remains neutral with regard to jurisdictional claims in published maps and institutional affiliations.



Open Access This article is licensed under a Creative Commons Attribution 4.0 International License, which permits use, sharing, adaptation, distribution and reproduction in any medium or format, as long as you give appropriate credit to the original author(s) and the source, provide a link to the Creative Commons license, and indicate if changes were made. The images or other third party material in this article are included in the article's Creative Commons license, unless indicated otherwise in a credit line to the material. If material is not included in the article's Creative Commons license and your intended use is not permitted by statutory regulation or exceeds the permitted use, you will need to obtain permission directly from the copyright holder. To view a copy of this license, visit <http://creativecommons.org/licenses/by/4.0/>.

This is a U.S. Government work and not under copyright protection in the US; foreign copyright protection may apply 2021